Draft version September 16, 2016
Preprint typeset using LaTeX style AASTeX6 v. 1.0

WATER ABSORPTION SIGNATURES IN REFLECTED LIGHT FROM CLOUDY COOL GIANT PLANETS

Ryan MacDonald[1]
Institute of Astronomy
University of Cambridge
Cambridge CB3 0HA, UK

Mark S. Marley
NASA Ames Research Center
Moffett Field, CA 94035, USA

Nikole K. Lewis
Space Telescope Science Institute
3700 San Martin Drive
Baltimore, MD 21218, USA

[1]r.macdonald@ast.cam.ac.uk

ABSTRACT

The presence of clouds or hazes is a fundamental challenge in the interpretation of transmission spectra, as they dampen spectral absorption features. In contrast, highly scattering clouds brighten reflected light spectra and enhance molecular absorption features at visible wavelengths. Water absorption is not seen in reflected light spectra of the solar system gas giants, due to rainout into the deep atmosphere, but is expected to manifest for even marginally warmer extrasolar planets. NASA's WFIRST mission will be able to observe reflected light spectra of a subset of known radial velocity planets, potentially allowing water abundances of true solar system analogues to be measured and hence constraining the C/O ratios of cool giant exoplanets. We generate over 1,000 theoretical reflected light spectra, including NH_3 and/or H_2O clouds, to investigate how the appearance and strength of water absorption signatures in cool giant planets vary as functions of effective temperature, sedimentation efficiency and gravity. For clouds similar to those of Jupiter ($T_{\rm eff}$ = 124 K), water absorption begins to appear around 0.94 μm for planets 50 K warmer and can alter the geometric albedo by factors > 2 in this band for temperatures 120 K warmer. Water absorption signatures are also seen around 0.83 μm and an entire series of features bluewards of 0.73 μm are especially visible for high sedimentation efficiency and low gravity - in some cases altering the geometric albedo by > 0.1 at these short wavelengths. When H_2O clouds are present, water absorption around 0.94 μm is strongest for planets with high temperature, low gravity and high sedimentation efficiency. We identify the planet HD 192310 c as a particularly promising target for detecting water in reflected light.

Keywords: planets and satellites: atmospheres

1. INTRODUCTION

Observations of exoplanetary spectra are beginning to provide unprecedented constraints on molecular abundances in the atmospheres of these distant worlds - for recent reviews, see Madhusudhan et al. (2014b, 2016). One of the most remarkable successes to date has been deriving precise constraints of the abundance of water in the atmospheres of close-in hot Jupiters (e.g. Kreidberg et al. 2014b, Madhusudhan et al. 2014a), which has not yet been accomplished for the gas giants in our own solar system. This difficulty stems from the fact that, at the much lower temperatures in the outer solar system ($T_{\rm eff}$ = 124 K for Jupiter), water condensation in the deep atmosphere depletes the H_2O vapour concentration in the observable atmosphere.

Water is of particular interest as, being one of the dominant volatiles in planet-forming regions, its abundance can serve as an important indicator of the processes that drive planetary formation (van Dishoeck et al. 2014) - permitting determination of C/O and O/H ratios when combined with values for the other dominant molecular species. In the case of Jupiter, core accretion models assuming a solar-composition nebula predict an enhanced water abundance of 3-7x the solar value (Mousis et al. 2012). However, in-situ measurements from the Galileo entry probe measured a water abundance of only 0.3x solar, compared to 2-3x solar for C, N, S, Ar, Kr and Xe (Wong et al. 2004) - though this O abundance is commonly seen as a lower limit, as the region probed is considered to be a dry spot in Jupiter's atmosphere. Taken at face value, such a low water abundance (which would imply C/O > 1) requires exotic formation conditions (see Lodders 2004 for an idea involving tarry planetesimals). It is hoped this question can ultimately be resolved, at least for Jupiter, by measurements of the water abundance in the Jovian atmosphere by NASA's Juno mission (Matousek 2007) which is, as of 2016, in operational orbit around Jupiter.

In the case of exoplanets, constraints from transmission spectroscopy of hot Jupiters have similarly been reported as suggestions of low water abundances (Madhusudhan et al. 2014a). Such inferences remain contested however, as dampened water absorption features can also be explained by invoking a high altitude opaque cloud deck (Sing et al. 2016). In raising the effective radius of the planet, the atmospheric annulus in which absorption features are imprinted is correspondingly reduced; leading to a flattening in the transmission spectrum (such as those reported by Kreidberg et al. 2014a; Knutson et al. 2014a,b; Ehrenreich et al. 2014). Indeed, it is becoming increasingly clear that clouds pose a fundamental challenge in the interpretation of chemical abundances derived from transmission spectra.

The apparent ubiquity of clouds in exoplanetary atmospheres need not be seen as a hopeless endeavour, as early theoretical studies of reflected light spectra revealed that clouds can enhance, rather than dampen, the visibility of absorption features in the optical (Marley et al. 1999; Sudarsky et al. 2000; Burrows et al. 2004; Sudarsky et al. 2005). This is due to backscattering of photons from highly reflective clouds enabling a fraction of those that would otherwise have been lost in the deep atmosphere to reach the observer, collecting absorption features along the way. Efforts are already underway to develop atmospheric retrieval techniques that could eventually utilise this scattering effect, offering the tantalising possibility of deriving the composition of true solar system analogues (Barstow et al. 2014; Lupu et al. 2016).

A number of these early studies identified an absorption feature due to water vapour in the vicinity of 0.94 μm - which coincides with the maximum water opacity in the optical - on warm ($T_{\rm eff} \sim 200$ K) giant planets (Marley et al. 1999; Sudarsky et al. 2000; Burrows et al. 2004). This feature is particularly interesting, as it was noted by Karkoschka (1994) as a possible explanation for a decrease in the disk-averaged reflected light of Jupiter observed between 0.92 - 0.95 0.95 μm - though this could also be due to ammonia (Karkoschka 1998). More recent studies have confirmed that water absorption in the optical is apparent for semi-major axes < 5 AU (Cahoy et al. 2010), sufficiently deep and thin water clouds (Morley et al. 2015) and could serve as a diagnostic for metallicity (Burrows 2014), but to date there has not been a thorough investigation as to when water absorption first becomes visible in the optical and how the strength of the feature varies in planetary parameter space. Such an investigation will prove advantageous for the purposes of identifying promising targets for NASA's Wide-Field InfraRed Survey Telescope (WFIRST) (Spergel et al. 2013); providing the ability to obtain directly imaged reflected light spectra of a subset of previously known radial velocity planets for the first time.

In this study, we begin the process of quantifying the role of water absorption in directly imaged cool giant planets observed in reflected light. Our investigation employs established radiative-convective equilibrium (Toon et al. 1989; McKay et al. 1989a), chemical equilibrium and clouds models (Ackerman & Marley 2001) to calculate reflected light spectra using the geometric albedo model presented in Cahoy et al. (2010) - itself built upon the model of Marley et al. (1999). In §2, we briefly review the role of ammonia and water clouds in cool giant planets by applying our suite of models to generate reflected light spectra of Jupiter. In §3, we summarise the essential physical basis of the models employed in this study, as well as explain our methodology in exploring the influence of water absorption in reflected light spectra. In §4, we present reflected light spectra for an ensemble of Jupiter analogues as a function of effective temperature, cloud properties and gravity. These are used in §4.2 to produce 2-D joint-parameter space contour maps quantifying the impact on reflected light spectra due to water absorption around 0.94 μm. In §4.3, we examine a number of promising radial velocity candidates for detecting water absorption signatures, generating representative theoretical reflected light spectra for each target of interest. Finally, in §5, we summarise our key conclusions, examine the assumptions inherent in our approach and discuss the implications for WFIRST target selection.

2. BACKGROUND

2.1. *Geometric Albedo*

When we refer to reflected light spectra in this work, we will generally express our results in terms of the associated *geometric albedo spectrum*. For historical reasons, this is defined as the ratio of the observed flux of scattered light from the planet at full phase (i.e. when the planet-star-observer angle is 180°) to that of an isotropically scattering disk of the same cross sectional area as the planet and placed at the same distance. Though this definition may not be particularly enlightening, it is equivalent to the far more intuitive relation (see Seager 2010, chap. 3):

$$A_g(\lambda) = \left(\frac{R_p}{d}\right)^{-2} \frac{F_p(\alpha = 0, \lambda)}{F_*(\lambda)} \tag{1}$$

where R_p is the planetary radius, d is the planet-star orbital separation, F_p is the scattered (i.e. reflected) light flux from the planet at zero phase angle and F_* is the observed stellar flux. Thus we can consider the geometric albedo spectrum to be essentially a measure of the planet-star flux ratio when the planetary hemisphere seen by the observer is fully illuminated. For partial illumination conditions (i.e. non-zero phase angles), the planet-star flux ratio is reduced and the left hand side of Eq. 1 is correspondingly multiplied by a phase function - normalised to 1 when $\alpha = 0$.

2.2. *Geometric Albedo Spectrum of Jupiter*

For demonstration purposes, in Figure 1 we illustrate the notion of geometric albedo spectra and the role of clouds in the familiar solar system context of Jupiter. The representative spectra here (generated using the suite of models described in §3) use the Jupiter pressure-temperature (PT) profile derived by Lindal et al. (1981) from Voyager radio occultation measurements and assume 3x solar metallicity. The non-cloudy model (red) is dominated by a Rayleigh slope towards short wavelengths with prominent absorption features due to CH_4. The model including H_2O and NH_3 clouds (green) is seen to be substantially brighter at longer wavelengths, which is a consequence of the high single-scattering albedos of these clouds. For comparative purposes, we also show the disk-averaged albedo spectrum of Jupiter obtained by Karkoschka (1994). The stark difference between our models and the observed spectrum at shorter wavelengths is due to our models not including photochemical hazes, such as exist in Jupiter's upper atmosphere (Marley et al. 1999; Sudarsky et al. 2000). Also note that we have not optimised molecular abundances or cloud properties with the intention to fit the observed spectrum, so the overall agreement is satisfactory.

Karkoschka (1994) noted that a slight decrease in Jupiter's albedo between 0.92 - 0.95 μm (highlighted) relative to Saturn could potentially be attributed to H_2O absorption - though it was later ascribed to NH_3 (Karkoschka 1998). To assess this we also generated a model spectrum in which each layer in the atmosphere had 100x less H_2O present (green dotted line), which is seen to be coincident over the entire wavelength range, even at the location of maximum

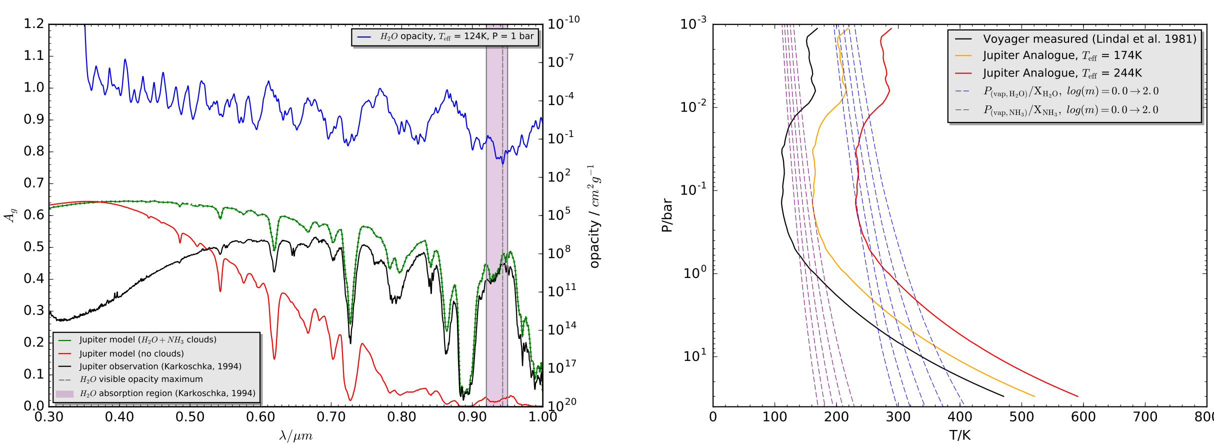

Figure 1. Left: Jupiter's geometric albedo spectrum with clouds (green), without clouds (red) and compared to the observed disk-integrated spectrum of Karkoschka (1994) (black). The coincident dotted green line indicates the spectrum if water vapour is removed. The highlighted region from 0.92 - 0.95 μm was suggested by Karkoschka (1994) as a water absorption feature. The dashed grey line indicates the location of the maximum water opacity (blue) in the visible. Right: pressure-temperature profiles of Jupiter (Lindal et al. 1981) (black) along with 50 K and 120 K warmer analogues (orange and red). The dashed lines are water (blue) and ammonia (purple) condensation curves for log metallicities 0.0, 0.5, 1.0, 1.5 and 2.0x solar.

water absorption in the optical around 0.943 μm, so our Jupiter reference model displays no signs of H_2O absorption.

To understand why this is the case, Jupiter's PT profile (Lindal et al. 1981) is plotted on the right of Figure 1 (black) vs. condensation curves for NH_3 (purple) (Ackerman & Marley 2001, Appendix A) and H_2O (blue) (Buck 1981). A cloud forms at the lowest point in the atmosphere where the partial pressure of a condensible species exceeds its saturation vapour pressure:

$$P(T)\,X_{v,i} \geq P_{\mathrm{vap},i}(T) \tag{2}$$

where $P(T)$ is the (total) atmospheric pressure in a given layer, $X_{v,i}$ is the mixing ratio of the vapour form of the condensing species i and $P_{\mathrm{vap},i}(T)$ is the corresponding vapour pressure curve. This is equivalent to finding the deepest layer in which the planetary PT profile intersects the condensation curve appropriate to the metallicity of the condensible species. Above this point, $X_{v,i}$ reduces due to rainout as the vapour forms. In the case of no intersection, the species will remain in gaseous form throughout the atmosphere. The shape of the PT profile thus governs both the altitude at which clouds form and the types of clouds present. For Jupiter, both ammonia clouds and water clouds are present at altitudes of ~100 mbar and ~5 bar respectively (intersection with the second H_2O condensation curve in Figure 1, corresponding to $10^{0.5} \approx 3$x solar). The depletion of H_2O due to rainout above the cloud base, which occurs sufficiently deep that few visible photons will reach, is the reason why no water absorption features are seen in Jupiter's geometric albedo spectrum.

We also display in Figure 1 two 'Jupiter analogue' PT profiles to illustrate the effect of raising the effective temperature of a planet. For this profile shape, raising the temperature of Jupiter by ~50 K (orange) removes the NH_3 clouds (Class I $\rightarrow$ Class II in the Sudarsky et al. (2000) classification scheme). Similarly, the H_2O clouds will begin to dissipate for $T_{\mathrm{eff}} \gtrsim 250$ K (Class II $\rightarrow$ Class III). Higher metallicity allows the clouds to persist to higher temperatures and pushes them deeper into the atmosphere. Due to the rising cloud base as a function of temperature, it is expected that the fraction of photons reaching the cloud, and hence those reflected towards the observer, will increase with temperature. These reflected 'deep' photons will accrue absorption features due to H_2O vapour encountered on their inbound and outbound journies, which will leave an imprint on the resulting geometric albedo. Our objective in this study is to examine when such features first become visible and how their strength varies as a function of effective temperature, cloud properties and gravity. We first turn to a description of the modelling methodology employed during this investigation.

3. METHODOLOGY

3.1. *Model Atmospheres*

Whilst, in principle, a radiative-convective equilibrium model could be produced for each point in parameter space, for the purposes of efficiently exploring this space at a reasonably high resolution (see §3.4), we elect to make a number of simplifying assumptions in the initial stage of this investigation. Firstly, we treat the planetary PT profile as a known function of effective temperature by linearly perturbing the Voyager measured Jupiter PT profile (sampled at 98 points between $\sim 10^{-3}$ and ~ 30 bar) from Lindal et al. (1981) by a constant temperature shift. For each resulting profile, we modify the chemical equilibrium mixing ratios of the condensing species (NH_3 and H_2O) from those corresponding to the fiducial (unperturbed) profile by starting at the base of the atmosphere and assuming all material in excess of the vapour pressure condenses (i.e. neglecting supersaturation) (Lewis 1969):

$$X_{v,i}(z) = \min[X_{v,i}(z - \Delta z), P_{\mathrm{vap},i}(z)/P(z)] \tag{3}$$

where z (or alternatively T) specifies the altitude and hence the atmospheric layer considered. The vapour pressure curves for water and ammonia, $P_{\mathrm{vap,\,H_2O}}$ and $P_{\mathrm{vap,\,NH_3}}$ used are those of Buck (1981) and (Ackerman & Marley 2001, Appendix A) respectively. Eq. 3 is used as a first-order correction to the vapour mixing ratios to account for the changing location of the cloud base with effective temperature - implemented to ensure a degree of consistency between the chemical abundances and the cloud profile generated for the new PT profile (§4). In all cases, the initial 'deep' abundances of H_2O, NH_3 and CH_4 are set to 3x solar, as is appropriate for Jupiter (Wong et al. 2004) - we take 'solar' to mean mixing ratios of $7.89\,\mathrm{x}\,10^{-4}$, $5.13\,\mathrm{x}\,10^{-4}$ and $1.42\,\mathrm{x}\,10^{-4}$ for H_2O, NH_3 and CH_4 respectively (Lodders 2003).

When considering specific known planets, we instead take a more rigorous approach. The PT profile is iteratively calculated assuming radiative-convective equilibrium, chemical equilibrium and the presence of clouds until a self-consistent fully-converged profile is identified (Morley et al. 2014). Radiative transfer is calculated using the two-stream approximation described in Toon et al. (1989) - the implementation of which and some applications can be found in McKay et al. (1989a,b); Marley et al. (1996); Burrows et al. (1997); Marley & McKay (1999); Marley et al. (2002); Saumon & Marley (2008); Fortney et al. (2008). Gas opacities are computed via the correlated-k method using opacities from Freedman et al. (2008), updated for ammonia (Yurchenko et al. 2011) and H_2 collisionally-induced opacity (Richard et al. 2012) as described in Saumon et al. (2012). The chemical species considered in the equilibrium calculations include: H_2, H, He, H_2O, NH_3, CH_4, CO, CO_2, N_2, H_2S, Na, K, VO and TiO.

3.2. *Cloud Model*

We consider H_2O and NH_3 clouds via the prescription presented in Ackerman & Marley (2001), whereby the upwards flux of condensate and vapour by turbulent mixing is balanced by the downwards flux of condensate due to sedimentation. This is expressed for each condensate by the condition:

$$-K_{zz}\frac{\partial X_t}{\partial z} - f_{\rm sed}\, w_*\, X_c = 0 \tag{4}$$

where K_{zz} is the vertical eddy diffusion coefficient, $X_t = X_v + X_c$ is the total mixing ratio of vapour and condensate of the species, $f_{\rm sed}$ is a tunable parameter called the *sedimentation efficiency* and w_* is the convective velocity scale. K_{zz} and w_* are both determined via mixing length theory, assuming the diffusion coefficient corresponding to free convective heat transport (Gierasch & Conrath 1985) is equal to K_{zz}. In convectively stable regions, a minimum value of $K_{zz} = 10^5\,{\rm cm}^2\,{\rm s}^{-1}$ is prescribed to account for sources of residual turbulence in radiative regions. When $f_{\rm sed}$ is specified, Eq. 4 can be solved for the condensate mixing ratio in each layer, assuming that all excess vapour condenses (Eq. 3). Physically, greater values of $f_{\rm sed}$ leads to more efficient rainout and hence thinner cloud profiles.

The particle size distribution for each condensate species is assumed to be lognormal:

$$\frac{dn}{dr} = \frac{N}{r\sqrt{2\pi}\,\ln\sigma_g}e^{-\frac{\ln^2(r/r_g)}{2\ln^2\sigma_g}} \tag{5}$$

where $n(r)$ is the number density of condensate particles with radii $< r$, N is the total number density for a given condensate, r_g is the geometric mean radius and σ_g is the geometric standard deviation (here set to be 2.0 throughout).

Interpreting $f_{\rm sed}\, w_*$ as the mass-weighted sedimentation velocity

$$f_{\rm sed}\, w_* = \frac{\int_0^\infty v_f(r)\, r^3 \frac{dn}{dr} dr}{\int_0^\infty r^3 \frac{dn}{dr} dr} \tag{6}$$

where $v_f(r)$ is the particle 'fall' speed at a given radius - calculated assuming viscous flow around spherical particles and corrected for kinetic effects (see Ackerman & Marley 2001, Appendix B) - allows r_g to be determined by evaluating the integrals in Eq. 6. Eq. 5 can similarly be integrated to obtain the normalisation constant N which, together with r_g, fully specifies the distribution in terms of the only remaining free parameter, $f_{\rm sed}$.

With the size distribution determined, the scattering properties of the clouds are calculated using Mie theory assuming spherical, homogeneous, particles. The complex refractive indices of water ice (Warren 1984) and ammonia (Martonchik et al. 1984) are used to evaluate the various Mie efficiencies at 2000 equally-spaced wavelengths from 0.3 - 1.0 μm. These are then integrated over the particle size distributions (Eq. 5) to produce the single scattering albedo, cloud optical depth and asymmetry parameter for each atmospheric layer as a function of wavelength.

3.3. *Geometric Albedo Calculation*

Once the PT profile and cloud profile has been determined, the geometric albedo is calculated using the approach developed by Toon et al. (1977, 1989); McKay et al. (1989a); Marley et al. (1999); Marley & McKay (1999) and extended to arbitary phase angles by Cahoy et al. (2010). In this approach, the planetary hemisphere as seen by the observer is divided into a number of plane-parallel facets, each of which represents a column in which 1-dimensional radiative transfer including multiple scattering is evaluated by the method used in Toon et al. (1989). Since stellar light is incident at different angles for each facet and the observing angle also differs, the reflected flux scattered towards the observer will vary with latitude and longitude. Chebyshev-Gauss integration over the hemisphere's two dimensional coordinate system is performed to average over viewing geometry and produce the geometric albedo (see Cahoy et al. 2010 for greater detail). We generate geometric albedo spectra at the same 2000 wavelengths used in the cloud model, before smoothing each spectrum with a Gaussian filter of standard deviation 0.00175 μm for display purposes.

3.4. *Perturbed Jupiter Model Grid*

Our model grid spans $T_{\rm eff} = 74 - 244$ K, $f_{\rm sed} = 1 - 18$ and $g = 10 - 100\,{\rm m\,s^{-1}}$. We run one grid of models in increments of $\Delta T_{\rm eff} = 10$ K and $\Delta f_{\rm sed} = 1$, holding g fixed at the value of Jupiter ($25\,{\rm m\,s^{-1}}$), and a separate grid with the same temperature variation, $f_{\rm sed} = 3$ (thought to be appropriate for Jupiter Ackerman & Marley 2001) but variable gravity in increments of $\Delta g = 10\,{\rm m\,s^{-1}}$. We calculate the geometric albedo spectrum twice at each location in parameter space; once with water present at the chosen metallicity (3x solar) and once with each layer depleted in water by a factor of 100. We quantify the influence of H_2O absorption on the resulting albedo spectrum by:

$$\alpha = \frac{\int_{\lambda_1}^{\lambda_2} A_{g,\,0.01{\rm x\,H_2O}}(\lambda)\; d\lambda - \int_{\lambda_1}^{\lambda_2} A_{g,\,{\rm H_2O}}(\lambda)\; d\lambda}{\int_{\lambda_1}^{\lambda_2} A_{g,\,0.01{\rm x\,H_2O}}\; d\lambda} \tag{7}$$

where $\lambda_1 = 0.889$ μm and $\lambda_2 = 0.989$ μm are chosen such that they are located in CH_4 bands where the effect of water opacity is negligible. This region includes the range noted by Karkoschka (1994) in which water absorption is expected to play a role. The fractional change in the integrated albedo in this window is taken as a figure of merit, which is computed for each point on our model grid. The resulting discrete points $\alpha(T_i, f_i)|_{g=25\,{\rm m\,s^{-1}}}$ and $\alpha(T_i, g_i)|_{f_{\rm sed}=3}$ are then interpolated using a rectangular bivariate spline of cubic order to produce contour maps (§4.2 of how the strength of the water absorption in this spectral region varies with $T_{\rm eff}$, $f_{\rm sed}$, and g.

The temperature range is chosen to span the full range from H_2O and NH_3 condensation to the transition effective temperature at which water will no longer condense (see Figure 1). Typical values of f_{sed} considered to date have varied from 1-3 for planets (Ackerman & Marley 2001) up to 6 for brown dwarfs (Stephens et al. 2009) and occasionally as high as 10 for some cool giant planets (Cahoy et al. 2010). Values as small as 0.01 have also been considered to explain the flat transmission spectrum of Kreidberg et al. (2014a) (Morley et al. 2015). We chose $f_{sed} = 1$ as our minimum boundary, as smaller values produce thick highly-extended clouds that lead to uniformly bright albedo spectra with few absorption features. The maximum value was chosen to encompass all currently physically plausible values. Similarly, the range for g was chosen to include the likely locations of a number of radial-velocity planets for which $M\sin(i)$ is known (since we do not know a priori which value of $f_{\rm sed}$ is appropriate to these planets, we prescribe the Ackerman & Marley 2001 estimated value for Jupiter).

3.5. *WFIRST Targets of Interest*

We use the results of the previous subsection (namely, the greatest values of α) to identify promising known radial-velocity planets for detailed analysis. In contrast to the perturbed Jupiter models, where clouds are generated using a stand-alone version of the Ackerman & Marley (2001) code (which is not strictly self-consistent), here we use a fully iterative prescription that couples our radiative-convective equilibrium model to the Ackerman & Marley (2001) cloud models until a converged solution is found. This ensures that the PT profile used for each planet is self-consistent with both the cloud structure and equilibrium chemical abundances. We generate geometric albedo spectra for each target, taking into account additional parameters neglected for simplicity in §3.4 (such as non-zero eccentricity and variable metallicity), in order to assess whether these targets may be amenable to WFIRST follow-up.

4. RESULTS

4.1. *Geometric Albedo Trends*

Figure 2 displays geometric albedo spectra for cloudy Jupiter analogues with $T_{\rm eff} = 124$, 164, 204 and 244 K, along with $f_{\rm sed}$ and g fixed at 3 and $25\,{\rm m\,s^{-1}}$ respectively and 3x solar metallicity. The most dominant absorption features, seen at 0.73 and 0.89 μm, are due to to gaseous CH_4 opacity. The presence of H_2O absorption features is indicated by the coloured shaded regions, which represents the difference in the geometric albedo spectrum for each value of $T_{\rm eff}$ when the water abundance is reduced by a factor of 100 throughout the atmosphere. As the PT profile crosses the threshold after which NH_3 can no longer condense (green), the albedo brightens significantly across the visible due to newly exposed highly reflective (single scattering albedo typically > 0.999) H_2O clouds. With increased temperature, the cloud base forms higher in the atmosphere (Figure 1, right) where the lower pressures makes fulfilling Eq. 2 more difficult; leading to a lower condensate mixing ratio at the cloud base. This in turn lowers the optical depth of the cloud, producing a reduction in the number of photon scattering events and hence a diminished albedo across the visible. This higher cloud results in a reduction of the strength of the CH_4 absorption features, as the column abundance of methane prior to encountering the cloud is smaller. On the other hand, the lower water condensate to vapour ratio above the clouds in the warmer planets dramatically increases the H_2O vapour column abundance, which manifests

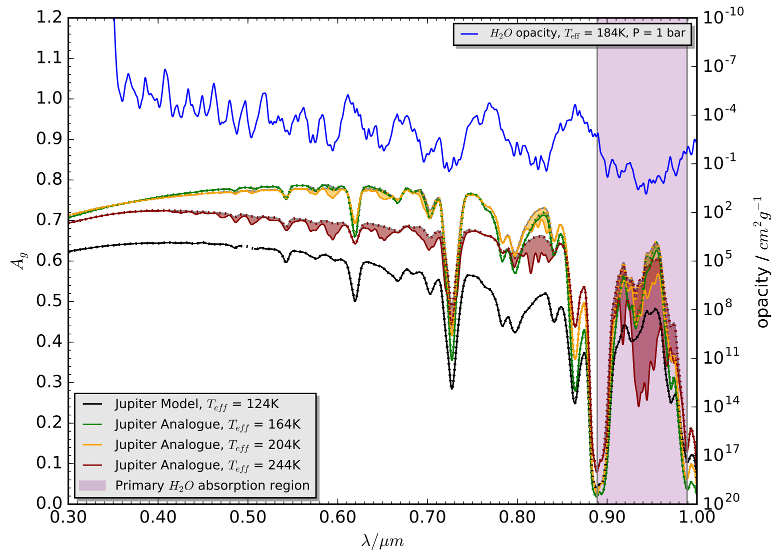

Figure 2. Geometric albedo spectra of a series of Jupiter Analogues ($f_{\rm sed} = 3$, $g = 25\,{\rm m\,s^{-1}}$ 3x solar) as a function of effective temperature. The black curve (the same as the cloudy model presented in Figure 1) corresponds to the same effective temperature as Jupiter, with the green, orange and red curves each warmer in increments of $\Delta T_{\rm eff} = 40K$. The blue curve shows the H_2O opacity evaluated at the average effective temperature of these four models and a representative pressure of 1 bar. Two curves are plotted for each value of $T_{\rm eff}$, with the dotted curve in each case an identical model in which the H_2O abundance is reduced by a factor of 100 throughout the atmosphere. The shaded area between each pair of curves is thus due to water absorption. The fractional change in the integrated albedo due to absorption in the highlighted spectral window between 0.889 μm and 0.989 μm, encapsulating the strongest H_2O absorption band in the optical, is used to derive the spectral index α (Eq. 7) for each parameter combination.

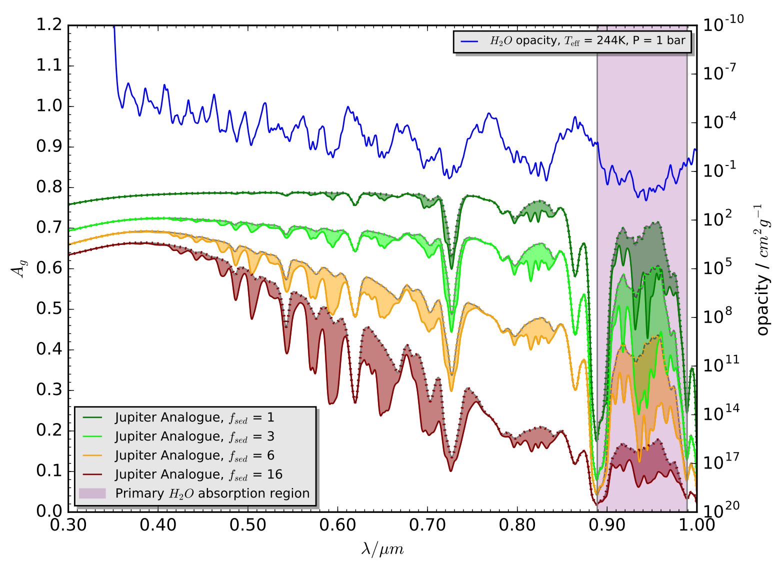

Figure 3. Geometric albedo spectra of a series of Jupiter Analogues ($g = 25\,{\rm m\,s^{-1}}$ 3x solar), each with $T_{\rm eff} = 244$ K, as a function of sedimentation efficiency. The green, lime, orange and red curves correspond to $f_{\rm sed} = 1$, 3, 6 and 16 respectively. For comparison purposes, note that the lime curve here corresponds to the same parameter combination as the red curve in Figure 2. The blue curve shows the H_2O opacity evaluated at the same temperature as the effective temperature of these four models and a representative pressure of 1 bar. Two curves are plotted for each value of $f_{\rm sed}$, with the dotted curve in each case an identical model in which the H_2O abundance is reduced by a factor of 100 throughout the atmosphere. The shaded area between each pair of curves is thus due to water absorption. The fractional change in the integrated albedo due to absorption in the highlighted spectral window between 0.889 μm and 0.989 μm, encapsulating the strongest H_2O absorption band in the optical, is used to derive the spectral index α (Eq. 7) for each parameter combination.

most strikingly around 0.94 μm as anticipated. Interestingly, a number of secondary water absorption signatures are also seen at ~ 0.83 μm and bluewards of the CH_4 feature around 0.73 μm for the highest temperatures considered. We see that, for sedimentation efficiencies and gravity analogous to Jupiter, water absorption first manifests for effective temperatures $\gtrsim 20$ K than the point at which NH_3 clouds dissipate, with the albedo in the heart of the 0.94 μm absorption feature altered by a factor of ~ 2 for planets with $\Delta T_{\rm eff} \gtrsim +100$ K relative to Jupiter.

Variation in the albedo spectrum with $f_{\rm sed}$ is depicted in Figure 3. For the purpose of clearly demonstrating trends with $f_{\rm sed}$, we fix the effective temperature of the plotted models at the value showing maximal H_2O absorption in Figure 2 (244 K). As in Figure 2, g is held at $25\,{\rm m\,s^{-1}}$ and metallicity is 3x solar. Models with $f_{\rm sed} = 1$, 3, 6 and 16 are displayed, such that the lime curves here correspond to the red curves in Figure 2. The general slopping behaviour of the albedo as higher values of $f_{\rm sed}$ is approached is similar to the Rayleigh-dominated spectra seen in cloud-free models (e.g. Figure 1, red curve). This effect is due to high $f_{\rm sed}$ resulting in thinner clouds localised deeper in the atmosphere, which causes optical depths to approach unity and hence tend towards cloud-free spectra as the probability of encountering the cloud deck rapidly becomes negligible. However, as the optical depth prior to encountering the cloud increases so too does the fractional change in the albedo in H_2O absorption features, particularly around 0.94 μm. Interestingly, we note that the series of absorption features at wavelengths < 0.73 μm become progressively more prominent with increased $f_{\rm sed}$, with a particularly strong feature around 0.59 μm that can change the geometric albedo by > 0.2 for values of $f_{\rm sed}$ around 16. As these features are located further up the Rayleigh slope, it may be the case that their detection prospects are enhanced relative to the much darker feature seen around 0.94 μm.

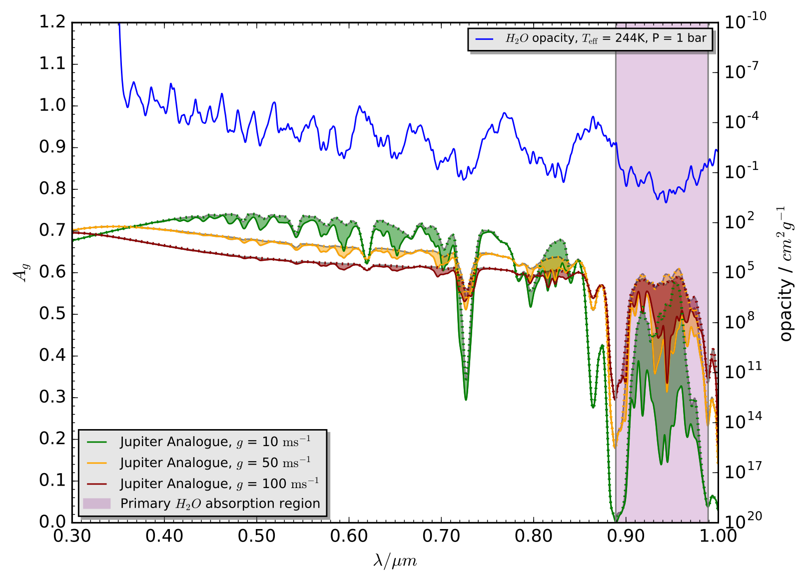

Figure 4. Geometric albedo spectra of a series of Jupiter Analogues ($f_{\rm sed} = 3$, 3x solar), each with $T_{\rm eff} = 244$ K, as a function of gravitational field strength. The green, orange and red curves correspond to $g = 10$, 50 and 100 ${\rm m\,s^{-1}}$ respectively. The blue curve shows the H_2O opacity evaluated at the same temperature as the effective temperature of these four models and a representative pressure of 1 bar. Two curves are plotted for each value of g, with the dotted curve in each case an identical model in which the H_2O abundance is reduced by a factor of 100 throughout the atmosphere. The shaded area between each pair of curves is thus due to water absorption. The fractional change in the integrated albedo due to absorption in the highlighted spectral window between 0.889 μm and 0.989 μm, encapsulating the strongest H_2O absorption band in the optical, is used to derive the spectral index α (Eq. 7) for each parameter combination.

The variation with gravitational field strength, as depicted in Figure 4, is comparatively more complicated. As with Figure 2, we fix $f_{\rm sed}$ at 3 and metallicity at 3x solar, in analogy with Jupiter, though at an enhanced $T_{\rm eff}$ of 244 K due to dampened absorption features at lower temperatures. Models with $g = 10$, 50 and 100 ${\rm m\,s^{-1}}$ are displayed. For this particular value of $T_{\rm eff}$, the albedo of the lowest gravity planets are enhanced at most visible wavelengths - though this trend is sensitive to temperature and we do not observe it to hold generally. The impact of H_2O absorption on the spectrum is seen to be greatest for lower gravity planets, which can be understood as being due to the enhanced scale height of the atmosphere proportionally raising the column abundance of H_2O encountered by reflected photons. This gravity enhancement is only apparent for the highest temperatures studied, as we explore in the following section.

4.2. *Water Absorption Contours*

We now turn to quantifying the qualitative 1-D parameter trends seen in the previous section. The approach employed is outlined in §3.4. We quantify H_2O absorption via the fractional integrated albedo between 0.889 μm and 0.989 μm, as the highly irregular shape of the albedo spectra in this region (see Figures 2, 3 and 4) renders such an average measure better suited than absolute differences in geometric albedo between fixed wavelengths 'inside' and 'outside' the feature.

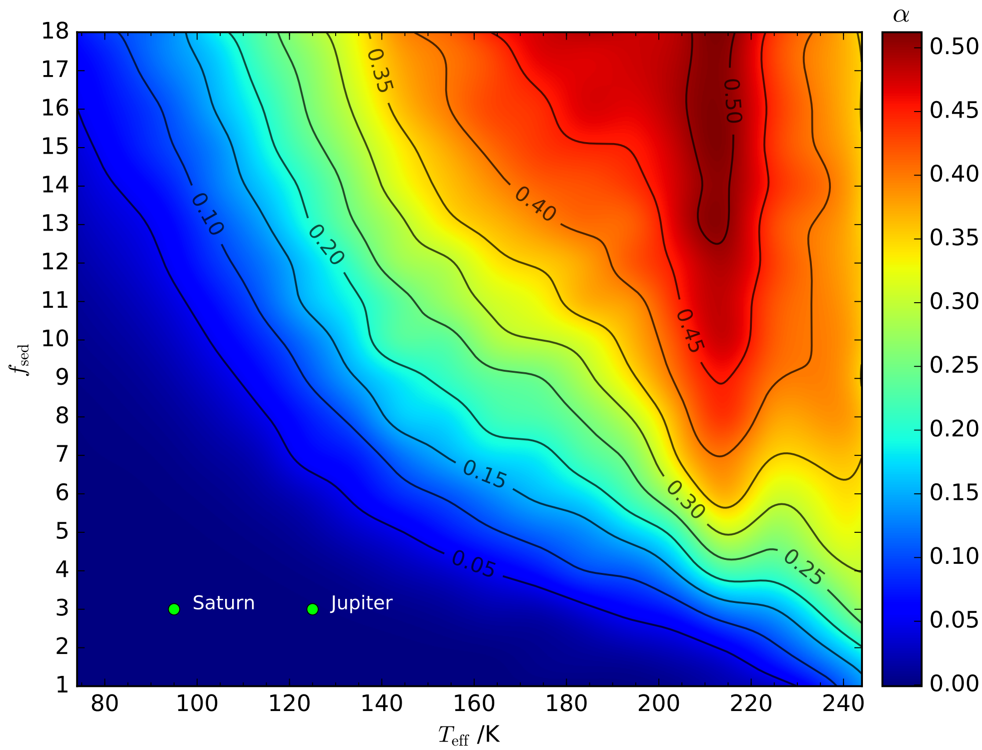

Figure 4. H_2O absorption strength as a function of T_{eff} and f_{sed} for a series of Jupiter analogues, each fixed with $g = 25$ m s^{-1} and 3x solar metallicity. The colour scale given is the fractional change in the integrated geometric albedo between 0.889 μm and 0.989 μm, which encapsulates the maximum water opacity in the visible. The approximate locations of Jupiter and Saturn in this plane are plotted, using the value of f_{sed} deduced by Ackerman & Marley (2001) to be appropriate for Jupiter.

Figure 4 shows a 2-D slice of parameter space in the $T_{eff} - f_{sed}$ plane, with g held at 25 m s^{-1} and metallicity at 3x solar, coloured in terms of the index α defined in Eq. 7. This can thus be considered a visual representation of the effect of H_2O absorption on the geometric albedo spectrum around 0.94 μm - with red colouration indicating strong influence due to water absorption signatures - as a function of temperature and cloud sedimentation efficiency. By overplotting Jupiter and Saturn on this plane, we see that they lie outside the region for which we expect H_2O absorption to play a prominent role role, which matches observations (Karkoschka 1994, 1998). It is interesting to note however that they appear to be located 'at the foot of the mountain', as either an increase in f_{sed} to 6 or an increase in T_{eff} by 60 K would be enough to place Jupiter in the region where we find a 5% change in the integrated albedo near the H_2O opacity maximum in the visible. As noted in §3.4, values of f_{sed} in the range 1-3 are commonly considered for giant planets (Ackerman & Marley 2001), though values as high as 10 have been explored (Cahoy et al. 2010). A maximum in the water absorption ($\alpha \sim 0.5$) is observed for $T_{eff} \sim 210$ K and $f_{sed} > 13$, which can be understood intuitively as follows: at high f_{sed} and temperatures below the maximum value of α, the base of the relatively compact cloud is located at large optical depths (e.g. $T_{eff} = 184$ K and $f_{sed} = 16$ has a cloud base at ~ 3 bar) whereas slightly higher temperatures ($T_{eff} \approx 214$ K) see the cloud become accessible to the majority of photons (cloud base at ~ 1 bar); going still higher reduces the H_2O vapour column abundance above the cloud and hence lowers the value of α. Generally speaking, this plot suggests higher values of T_{eff} and f_{sed} will be most amenable to detection and abundance measurements of water vapour.

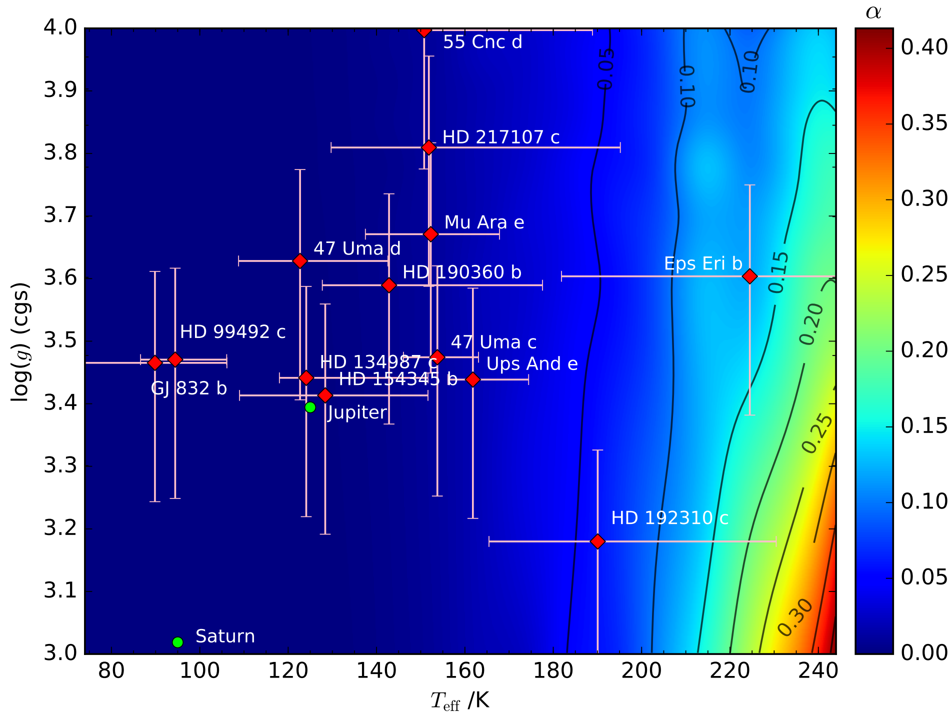

Figure 5. H_2O absorption strength as a function of $T_{\rm eff}$ and g for a series of Jupiter analogues, each fixed with $f_{\rm sed} = 3$ and 3x solar metallicity. The colour scale given is the fractional change in the integrated geometric albedo between 0.889 μm and 0.989 μm, which encapsulates the maximum water opacity in the visible. Overplotted are the locations of Jupiter and Saturn in this plane, along with the approximate locations of a selection of radial velocity targets that could potentially be observed by WFIRST. The plotted gravity of each planet is obtained by setting $M\sin(i)$ of each planet equal to M and deriving radii by assuming $R = R_J$ for $M > M_J$ and linearly interpolating radii between that of Jupiter and Neptune over the corresponding mass range for $M < M_J$. The vertical error bars in g come from ascribing an uncertainty of 20% in the assumed planetary radius. The values of $T_{\rm eff}$ and horizontal error bars are derived from giant planet cooling models, accounting for eccentricity variations and assuming a 100% error in the system age.

Figure 5 explores a similar 2-D slice of parameter space, this time in the $T_{\rm eff} - g$ plane, with $f_{\rm sed}$ held at 3 and metallicity at 3x solar. A clear sloping behaviour is seen, with maximal values of α in this plane arising from a combination of high $T_{\rm eff}$ coupled with low g. This gravity enhancement is weak, as seen by the nearly vertical 5% contour, though becomes stronger with increasing temperature (the contours begin to slope strongly once $T_{\rm eff} \gtrsim$ 210 K. This temperature-dependant gravity enhancement can be understood in terms of the changing scale height of the atmosphere: for cool planets on the left of the figure, such as Jupiter, few photons reach the deep regions with significant water vapour and so increasing the scale height (by lowering g) has little effect on α. Warmer planets, however, have sufficiently high cloud decks that backscattered photons will encounter sufficient water vapour to imprint on the spectrum; increasing the scale height of such planets relative to the photon mean free path naturally leads to an increasing number of interactions with H_2O molecules and thus water absorption features become more apparent. For reference, we overplot the locations of Jupiter and Saturn in this plane, along with approximate locations of a number of radial velocity planets that WFIRST could potentially observe (assuming $f_{\rm sed} = 3$ for each). As g for these planets are not known, due to a lack of radii measurements, we set $R = R_J$ for $M > M_J$ and linearly interpolate radii between that of Jupiter and Neptune over the corresponding mass range for $M < M_J$. We also assume $M\sin i \approx M$, subsuming errors from this crude approach into a 20% error on the radius. The values of $T_{\rm eff}$ and their corresponding errors are derived from giant planet cooling models, accounting for eccentricity variations and assuming a 100% error in the system age.

The combined effect of Figures 4 and 5 can be visualised in 3-D as a succession of $T_{\rm eff} - f_{\rm sed}$ planes where the maximum α contour progressively shifts to higher values of $T_{\rm eff}$ and stretches towards higher temperatures (due to gravity enhancement) as slices with lower values of g are explored. Taken together, these figures suggest that the radial velocity planets with the greatest potential for H_2O absorption to be observed are *Epsilon Eridani b* and *HD 192310 c*, which we now turn our attention towards.

4.3. *WFIRST Target Albedo Spectra*

4.3.1. *Epsilon Eridani b*

At a nearby distance of 3.22 pc, Epsilon Eridani b (hereafter Eps Eri b) presents an intriguing target for direct imaging follow-up. Having been observed via both radial velocity and astrometric measurements, Eps Eri b's key properties have been determined to be: $M = 1.55 \pm 0.24\ M_J$, $a = 3.39$ AU, $e = 0.70$ and $P = 6.85 \pm 0.02$ yr (Benedict et al. 2006). The effective temperature from our evolution models is found to be $T_{\rm eff} = 224.49^{+55.36}_{-42.63}$ K. The highly eccentric orbit is of note, as it could potentially lead to clouds varying (or disappearing entirely) as a function of orbital separation (Burrows et al. 2004).

Our reference model for Eps Eri b sets $f_{\rm sed} = 6$, $g = 33.5\ {\rm m\,s^{-1}}$ and assumes solar metallicity; we then generate converged radiative-convective equilibrium PT profiles as a function of orbital separation for $d = 0.98$, 1.50 and 5.80 AU, along with the corresponding consistent cloud profile for each model. The results are shown in Figure 6, along with a representative Jupiter analogue with similar parameters ($T_{\rm eff} = 224$ K, $f_{\rm sed} = 6$, $g = 25\ {\rm m\,s^{-1}}$, 3x solar metallicity) for comparison purposes.

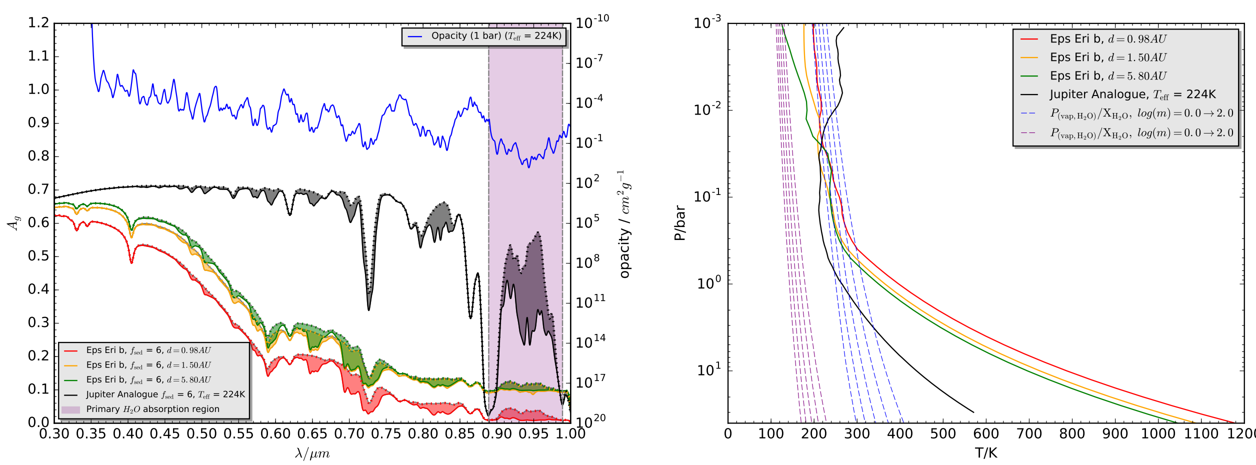

Figure 6. Left: Ep Eri b model geometric albedo spectra as a function of orbtial seperation, spanning $d = 0.98$ AU (red), 1.50 AU (orange) and 5.80 AU (green). Each model has $f_{\rm sed} = 6$, $g = 33.5\ {\rm m\,s^{-1}}$ and solar metallicity. The black curve is the closest Jupiter analogue for reference: $T_{\rm eff} = 224$ K, $f_{\rm sed} = 6$, $g = 25\ {\rm m\,s^{-1}}$ and 3x solar metallicity. The blue curve shows the H_2O opacity evaluated near the average effective temperature of Eps Eri b and at a representative pressure of 1 bar. Two curves are plotted for each model, with the dotted curve in each case an identical model in which the H_2O abundance is reduced by a factor of 100 throughout the atmosphere. The shaded area between each pair of curves is thus due to water absorption. The highlighted spectral window between 0.889 μm and 0.989 μm encapsulates the strongest H_2O absorption band in the optical. Right: radiative-convective equilibrium pressure-temperature profiles corresponding to our three Eps Eri b models (red, orange and green), along with the closest Jupiter analogue (black). The dashed lines are water (blue) and ammonia (purple) condensation curves for log metallicities 0.0, 0.5, 1.0, 1.5 and 2.0x solar.

Figure 6 shows clear signs of H_2O absorption features, particularly around local opacity maxima at ~ 0.65, 0.70, 0.83 and 0.94 μm, as were noted in our perturbed Jupiter analysis. However, the absolute level of the spectra is substantially lower than the corresponding Jupiter analogue at longer wavelengths with the overall shape characteristic of a Rayleigh slope towards the blue. This striking difference can be understood by contrasting the PT profiles (Figure 6, right), which cross the solar H_2O condensation curve (leftmost blue dashed line) at pressures $< 10^{-1}$ bar, compared to ~ 1 bar for the Jupiter analogue, resulting in high altitude thin clouds that do not efficiently scatter photons and hence the resemblance to cloud-free albedo spectra. Though flattening of the albedo spectra in the highlighted region due to water absorption is observed (with values of $\alpha = 0.611$, 0.122 and 0.110 for $d = 0.98$, 1.50 AU and 5.80 AU), the low albedo values ($A_g \lesssim 0.1$) suggests this would be an extremely challenging observation. Prospects are somewhat enhanced at shorter wavelengths, with the absorption feature around 0.65 μm offering a characteristic deviation from a straight line that could be amenable to spectral indexing. Overall though, the dark albedo of Eps Eri b leads us to conclude that this is not the best target for WFIRST follow-up.

4.3.2. *HD 192310 c*

The HD 192310 system, 8.82 pc away, contains another potentially promising planet - HD 192310 c. Properties of this planet determined by radial velocity measurements include: $M\sin(i) = 0.076 \pm 0.016\ M_J$, $a = 1.18 \pm 0.025$ AU, $e = 0.32 \pm 0.11$ and $P = 525.8 \pm 9.2$ day (Pepe et al. 2011). The effective temperature from our evolution model is found to be $T_{\rm eff} = 190.06^{+40.40}_{-24.61}$ K.

Our reference model for HD 192310 c sets $f_{\rm sed} = 3$, $g = 3.72\ {\rm m\,s^{-1}}$ and allows variable metallicity; we then generate converged radiative-convective equilibrium PT profiles as a function of metallicity for $\log(m) = 0.0$, 0.5, 1.0, 1.5 and 1.7, along with the corresponding consistent cloud profile for each model. The results are shown in Figure 7, along with a representative Jupiter analogue with similar parameters ($T_{\rm eff} = 194$ K, $f_{\rm sed} = 3$, $g = 10\ {\rm m\,s^{-1}}$, 3x solar metallicity) for comparison purposes.

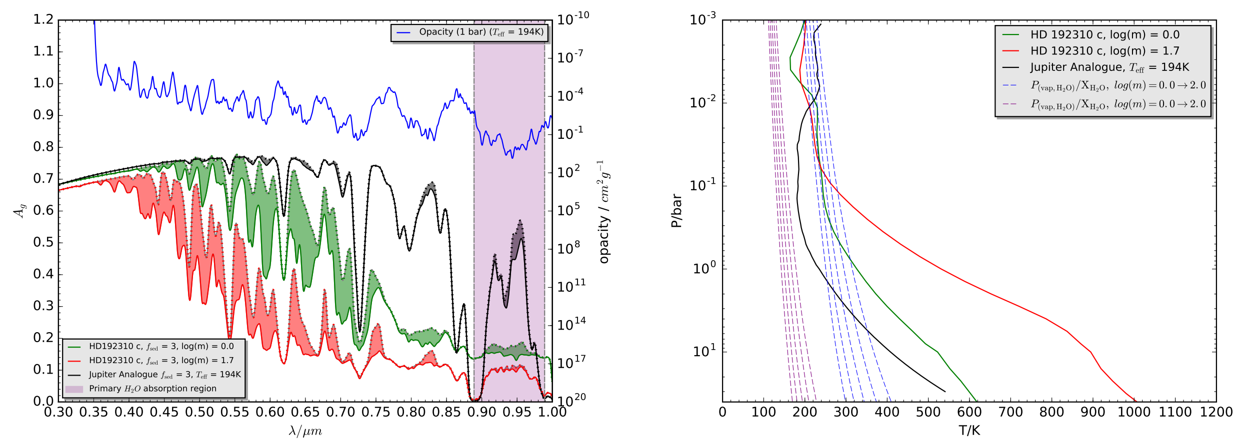

Figure 7. Left: HD 192310 c model geometric albedo spectra as a function of metallicity, with a 'metal poor', solar, model (green) and a 'metal rich', 50x solar, model (red) shown. Each model has $f_{\rm sed} = 3$ and $g = 3.72\ {\rm m\,s^{-1}}$. The black curve is the closest Jupiter analogue for reference: $T_{\rm eff} = 194$ K, $f_{\rm sed} = 3$, $g = 10\ {\rm m\,s^{-1}}$ and 3x solar metallicity. The blue curve shows the H_2O opacity evaluated near the effective temperature of HD 192310 c and at a representative pressure of 1 bar. Two curves are plotted for each model, with the dotted curve in each case an identical model in which the H_2O abundance is reduced by a factor of 100 throughout the atmosphere. The shaded area between each pair of curves is thus due to water absorption. The highlighted spectral window between 0.889 μm and 0.989 μm encapsulates the strongest H_2O absorption band in the optical. Right: radiative-convective equilibrium pressure-temperature profiles corresponding to the metal poor (green) and metal rich (red) HD 192310 c models, along with the closest Jupiter analogue (black). The dashed lines are water (blue) and ammonia (purple) condensation curves for log metallicities 0.0, 0.5, 1.0, 1.5 and 2.0x solar.

Though sloped towards the blue in a similar manner to our spectra of Eps Eri b (due to the high intersection points with the relevant condensation curves), Figure 7 demonstrates in contrast that H_2O absorption features are a major component in the overall shape of the geometric albedo spectra of HD 192310 c. This is in large part due to the remarkably low value of g for this planet, which produces a significant gravitational enhancement in the absorption features (as predicted in §4.1 and §4.2). Excellent agreement is obtained between the value of α for the HD 192310 c 3x solar model (0.065, not plotted) vs. that obtained for the closest Jupiter analogue (0.066), though the low value of A_g around 0.94 μm may again make this difficult to observe. However, the greatest contrasts between the models with H_2O and depleted in H_2O are seen for $\lambda \lesssim 0.73\ \mu$m, with a 'forest' of water absorption features appearing along the Rayleigh slope for every value of metallicity studied. These unexpectedly strong water absorption features suggest that HD 192310 c should be considered a priority target for WFIRST spectroscopy.

5. DISCUSSION

We have conducted an initial investigation into the appearance of water absorption signatures in reflected light from cool giant planets over the range $0.3\mu m \leq \lambda \leq 1.0\mu m$. By perturbing the PT profile of Jupiter, we were able to generate geometric albedo spectra across a 3-D parameter space spanned by effective temperature, cloud sedimentation efficiency and gravitational field strength. These results were used to inform the choice of two specific planets with potentially strong H_2O absorption features, for which we computed specific reflected light spectra: Epsilon Eridani b and HD 192310 c. This detailed modelling concluded that HD 192310 c is the most promising target, with a particularly strong series of H_2O absorption features at wavelengths $< 0.73\mu$m (Figure 7), thus we suggest it should be considered a priority target for WFIRST observations.

Our perturbed Jupiter analysis observed that the strength of water absorption in the vicinity of the maximum H_2O opacity in the visible (0.94 μm) is maximised for high $T_{\rm eff}$, high $f_{\rm sed}$ and low g (see Figures 4 and 5). Specifically, we observed that values of $f_{\rm sed} > 6$ or $T_{\rm eff} \gtrsim 184$ K result in the appearance of water absorption at the 5% level between 0.889 μm and 0.989 μm. This absorption can increase in strength to 50% or higher around $T_{\rm eff} = 210$ K and $f_{\rm sed} < 13$. Lowering g from that of Jupiter enhances these features for $T_{\rm eff} \gtrsim 180$ K by increasing the scale height of the atmosphere.

Though these results are illustrative for the purposes of target selection, we caution against the use of parameter space exploration such as this as a substitute for detailed modelling of individual planets. This was illustrated in the case of Epsilon Eridani b, for which the resulting albedo spectrum was morphologically quite distinct from that of a corresponding Jupiter analogue with similar values of $T_{\rm eff}$, $f_{\rm sed}$ and g - in large part due to the specific planetary PT profile crossing the H_2O condensation curve much higher in the atmosphere. Indeed, one of the limitations inherent in our perturbed Jupiter approach was assuming that the PT profile was a 'known' function of temperature, when in reality its shape will of course vary with other parameters such as metallicity, gravity and, in the case of clouds, sedimentation efficiency.

Our identification of HD 192310 c as a promising target for observing water absorption features is intriguing, not least due to the most dominant H_2O absorption signatures appearing at local opacity maxima shortwards of 0.73 μm, rather than around the visible opacity maximum around 0.94 μm as was initially expected. However, there are a few caveats worthy of further consideration that may influence the magnitude and detectability of such absorption signatures. Foremost, our models do not include the effect of photochemical hazes which can significantly darken the geometric albedo at wavelengths $\lesssim 0.6\mu$m (Marley et al. 1999; Sudarsky et al. 2000) (see also Figure 1). We have also assumed the abundances of non-condensing species are dictated by chemical equilibrium throughout this work, thus effects such as vertical-mixing (that can alter, for instance, the CH_4 abundance) are neglected. Furthermore, in reality the planet-star flux ratio will be less than that given by the geometric albedo via Eq. 1, as the planet is obscured by the star at zero-phase and would likely be observed at maximum angular separation (i.e. quarter-phase). Under such partial illumination conditions, the phase function can lower the flux ratio by a factor of 3-4 around 0.55 μm and 0.75 μm (Sudarsky et al. 2005) - compared to a factor of π for a perfectly isotropically scattering sphere.

A logical extension to our exploratory study would be to assess the feasibility of detecting H_2O absorption features for an emsemble of planets using simulated WFIRST spectra in a statistically robust manner. Due to the complicated morphology of the albedo spectra in the vicinity of water absorption features, traditional approaches whereby spectral indices are defined based on extrapolating a 'continuum' across a feature and ratioing this value with the observed albedo (e.g. Allers & Liu 2013) are poorly suited here. Indeed, the sensitivity of the shape to a wide range of physical parameters, such as gravity and metallicity, strongly indicates that the most viable approach here would be a Bayesian analysis whereby these 'nuisance' parameters can be properly marginalised over. Depending on the precision of the data, such an approach could be used to retrieve constraints on the H_2O abundance of these cool giant planets. Atmospheric retrieval techniques using reflected light are under active development (Barstow et al. 2014; Lupu et al. 2016), but have not yet been used to explore the possibility of constraining the H_2O abundance on these cool giant planets. The work carried out here indicates that water absorption signatures can significantly alter the albedo spectrum of a subset of these planets across multiple wavelength bands, and thus the prospects for detecting and measuring H_2O abundances appears to be bright indeed.

Much of the work contained in this study was conducted at the Kavli Summer Program in Astrophysics, which was enabled in large part by grants provided by The Kavli Foundation along with funding from The National Science Foundation, UCSC's Other Worlds Laboratory and UC Santa Cruz. We would like to explicitly acknowledge P. Garaud, the program coordinator, the Scientific Organising Committe (J. Fortney, D. Abbot, C. Goldblatt, R. Murray-Clay, D. Lin, A. Showman and X. Zhang), the Senior Lecturers (J. Bean, D. Catling and K. Menou) along with the Local Organising Committe (J. Scarpelli, Z. Kornber and S. Nasab) for crafting an experience that was as scientifically intense as it was socially rewarding. Finally, we thank the Kavli Fellows (A. Baker, C. Leung, C. Cadiou, D. Poell, G. McDonald, K. Feng, K. Ohno, L. Mayorga, M. Malik, N. Batalha, N. Espinoza, P. Gao, R. Garland, T. Komacek, T. Louden and Y. Kawashima) for exemplifying the spirit of exploration as we seek to understand strange new worlds.

REFERENCES

Ackerman, A. S., & Marley, M. S. 2001, ApJ, 556, 872

Allers, K. N., & Liu, M. C. 2013, Astrophys. J., 772, 79

Barstow, J. K., Aigrain, S., Irwin, P. G. J., et al. 2014, ApJ, 786, 154
Benedict, G. F., McArthur, B. E., Gatewood, G., et al. 2006, Astron. J., 132, 2206
Buck, A. L. 1981, J. Appl. Meteorol., 20, 1527
Burrows, A. 2014, ArXiv e-prints, arXiv:1412.6097
Burrows, A., Sudarsky, D., & Hubeny, I. 2004, ApJ, 609, 407
Burrows, A., Marley, M., Hubbard, W. B., et al. 1997, ApJ, 491, 856
Cahoy, K. L., Marley, M. S., & Fortney, J. J. 2010, ApJ, 724, 189
Ehrenreich, D., Bonfils, X., Lovis, C., et al. 2014, Astron. Astrophys., 570, A89
Fortney, J. J., Marley, M. S., Saumon, D., & Lodders, K. 2008, ApJ, 683, 1104
Freedman, R. S., Marley, M. S., & Lodders, K. 2008, Astrophys. J. Suppl. Ser., 174, 504
Gierasch, P. J., & Conrath, B. J. 1985, Energy conversion processes in the outer planets (Cambridge and New York: Cambridge University Press), 121–146
Karkoschka, E. 1994, Icarus, 111, 174
—. 1998, Icarus, 133, 134
Knutson, H. A., Benneke, B., Deming, D., & Homeier, D. 2014a, Nature, 505, 66
Knutson, H. A., Dragomir, D., Kreidberg, L., et al. 2014b, ApJ, 794, 155
Kreidberg, L., Bean, J. L., Désert, J.-M., et al. 2014a, Nature, 505, 69
Kreidberg, L., Bean, J. L., Dsert, J.-M., et al. 2014b, The Astrophysical Journal Letters, 793, L27
Lewis, J. S. 1969, Icarus, 10, 365
Lindal, G. F., Wood, G. E., Levy, G. S., et al. 1981, J. Geophys. Res. Sp. Phys., 86, 8721
Lodders, K. 2003, ApJ, 591, 1220
—. 2004, ApJ, 611, 587
Lupu, R. E., Marley, M. S., Lewis, N., et al. 2016, ArXiv e-prints, arXiv:1604.05370
Madhusudhan, N., Agúndez, M., Moses, J. I., & Hu, Y. 2016, Space Sci. Rev., 1
Madhusudhan, N., Crouzet, N., McCullough, P. R., Deming, D., & Hedges, C. 2014a, ApJ, 791, L9
Madhusudhan, N., Knutson, H., Fortney, J., & Barman, T. 2014b, Protostars Planets VI, pp 739
Marley, M. S., Gelino, C., Stephens, D., Lunine, J. I., & Freedman, R. 1999, ApJ, 513, 879
Marley, M. S., & McKay, C. P. 1999, Icarus, 138, 268
Marley, M. S., Saumon, D., Guillot, T., et al. 1996, Science, 272, 1919
Marley, M. S., Seager, S., Saumon, D., et al. 2002, ApJ, 568, 335
Martonchik, J. V., Orton, G. S., & Appleby, J. F. 1984, Appl. Opt., 23, 541
Matousek, S. 2007, Acta Astronaut., 61, 932
McKay, C. P., Pollack, J. B., & Courtin, R. 1989a, Icarus, 80, 23
—. 1989b, Icarus, 80, 23
Morley, C. V., Fortney, J. J., Marley, M. S., et al. 2015, ApJ, 815, 22
Morley, C. V., Marley, M. S., Fortney, J. J., et al. 2014, ApJ, 787, 21
Mousis, O., Lunine, J. I., Madhusudhan, N., & Johnson, T. V. 2012, ApJL, 751, L7
Pepe, F., Lovis, C., Ségransan, D., et al. 2011, Astron. Astrophys., 534, A58
Richard, C., Gordon, I., Rothman, L., et al. 2012, J. Quant. Spectrosc. Radiat. Transf., 113, 1276
Saumon, D., & Marley, M. S. 2008, ApJ, 689, 1327
Saumon, D., Marley, M. S., Abel, M., Frommhold, L., & Freedman, R. S. 2012, ApJ, 750, 74
Seager, S. 2010, Exoplanet Atmospheres: Physical Processes (Princeton University Press)
Sing, D. K., Fortney, J. J., Nikolov, N., et al. 2016, Nature, 529, 59
Spergel, D., Gehrels, N., Breckinridge, J., et al. 2013, ArXiv e-prints, 190
Stephens, D. C., Leggett, S. K., Cushing, M. C., et al. 2009, ApJ, 702, 154
Sudarsky, D., Burrows, A., Hubeny, I., & Li, A. 2005, ApJ, 627, 520
Sudarsky, D., Burrows, A., & Pinto, P. 2000, ApJ, 538, 885
Toon, O. B., B. Pollack, J., & Sagan, C. 1977, Icarus, 30, 663
Toon, O. B., McKay, C. P., Ackerman, T. P., & Santhanam, K. 1989, J. Geophys. Res., 94, 16287
van Dishoeck, E. F., Bergin, E. A., Lis, D. C., & Lunine, J. I. 2014, in Protostars Planets VI (University of Arizona Press), 835858
Warren, S. G. 1984, Appl. Opt., 23, 1206
Wong, M. H., Mahaffy, P. R., Atreya, S. K., Niemann, H. B., & Owen, T. C. 2004, Icarus, 171, 153
Yurchenko, S. N., Barber, R. J., & Tennyson, J. 2011, MNRAS, 413, 1828

ALL AUTHORS AND AFFILIATIONS

Ryan MacDonald[1],
Institute of Astronomy
University of Cambridge
Cambridge CB3 0HA, UK

Mark S. Marley,
NASA Ames Research Center
Moffett Field, CA 94035, USA

And
Nikole K. Lewis.
Space Telescope Science Institute
3700 San Martin Drive
Baltimore, MD 21218, USA

[1] r.macdonald@ast.cam.ac.uk